Conduction Band Fine Structure in Colloidal HgTe Quantum Dots

Margaret Hudson, Menglu Chen, Vladislav Kamysbayev, Eric Janke, Xinzheng Lan, Guy Allan, Christophe Delerue, Byeongdu Lee, Philippe Guyot-Sionnest, Dmitri Talapin

Conduction Band Fine Structure in Colloidal HgTe Quantum Dots

Margaret H. Hudson,[†] Menglu Chen,[‡] Vladislav Kamysbayev,[†] Eric M. Janke,[†] Xinzheng Lan,[†] Guy Allan,[§] Christophe Delerue,[§] Byeongdu Lee,[∥] Philippe Guyot-Sionnest,[†‡] Dmitri V. Talapin*[†⊥]

[†]*Department of Chemistry, James Franck Institute, and* [‡]*Department of Physics, James Franck Institute, University of Chicago, Chicago, Illinois 60637, United States*

[§]*Univ. Lille, CNRS, Centrale Lille, ISEN, Univ. Valenciennes, UMR 8520 - IEMN, F-59000 Lille, France*

[∥]*Advanced Photon Source and* [⊥]*Center for Nanoscale Materials, Argonne National Laboratory, Argonne, Illinois 60439, United States*

*E-mail: dvtalapin@uchicago.edu

ABSTRACT

HgTe colloidal quantum dots (QDs) are of interest because quantum confinement of semimetallic bulk HgTe allows one to synthetically control the bandgap throughout the infrared. Here, we synthesize highly monodisperse HgTe QDs and tune their doping both chemically and electrochemically. The monodispersity of the QDs was evaluated using small-angle x-ray scattering (SAXS) and suggests a diameter distribution of ~10% across multiple batches of different sizes. Electron-doped HgTe QDs display an intraband absorbance and bleaching of the first two excitonic features. We see splitting of the intraband peaks corresponding to electronic transitions from the occupied $1S_e$ state to a series of nondegenerate $1P_e$ states. Spectroelectrochemical studies reveal that the degree of splitting and relative intensity of the intraband features remain constant across doping levels up to two electrons per QD. Theoretical modeling suggests that the splitting of the $1P_e$ level arises from spin-orbit coupling and reduced

QD symmetry. The fine structure of the intraband transitions is observed in the ensemble studies due to the size uniformity of the as-synthesized QDs and strong spin-orbit coupling inherent to HgTe.

Keywords: colloidal quantum dots, doping, infrared, electronic structure, spectroelectrochemistry

TABLE OF CONTENTS GRAPHIC

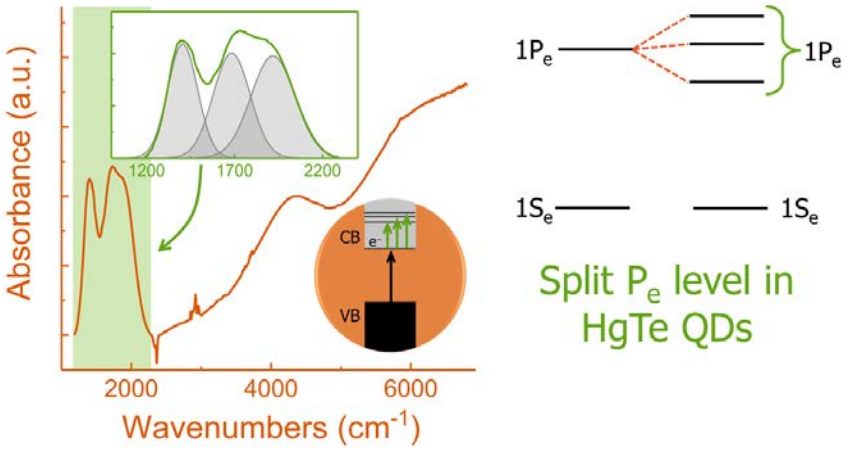

Colloidal semiconductor nanocrystals have outstanding optoelectronic properties that can be readily tuned through manipulation of nanocrystal size, shape, and surface passivation. Semiconductor nanocrystals smaller than the Bohr exciton radius, termed quantum dots (QDs), display size-dependent absorption and emission. Much work has focused on the development of colloidal QDs as spectrally narrow absorbers and emitters in the visible and near-infrared (IR) for use in light emission,[1, 2, 3] photovoltaics,[4, 5, 6] and solar concentrators.[7, 8] To extend sensitivity into the mid- to far-IR, colloidal QD syntheses of narrow bandgap semiconductors (InSb,[9] PbSe[10]) and semimetals (HgSe,[11] HgTe,[12, 13] Cd_3As_2[14, 15]) have been established. Developments in the synthesis of HgTe QDs have yielded routes to size-uniform, narrow absorbers from the near- to far-IR.[13, 16, 17, 18] These HgTe QDs show remarkable performance as the active layer in solution-processed infrared photodetectors,[12, 19] reaching background-limited performance in photovoltaic devices.[20, 21, 22]

In addition to QD size control and corresponding spectral tuning, device applications of QDs require precise control over the electronic doping of a QD ensemble. Delocalized electrons can be introduced into the quantum confined states of a QD sample electrochemically[23, 24, 25] or chemically, through reaction with a reducing agent,[26] sometimes accompanied by photoexcitation.[27] However, such doping is often transient; the nanocrystals relax back to their undoped state upon removal of the applied bias or over time. Stable nanocrystal doping can be achieved through incorporation of aliovalent impurities into the lattice (*e.g.* Al^{3+} in ZnO[28]) or by tuning the potential of the electronic states with respect to the environment through modification of the QD surface chemistry.[29, 30] These additional electrons reside in discrete, quantum confined states derived from the conduction band of the bulk semiconductor (here referred to as

conduction band states). The presence of electrons in the first conduction band state, the $1S_e$ state, of a QD sample can be identified spectroscopically by the suppression of band-edge absorption due to Pauli blocking and the emergence of intraband absorbance significantly below the QD bandgap due to excitations from the doped state to higher energy states.

Mercury chalcogenide (HgE, E = S, Se, Te) QDs are a rich system for the exploration of electronic doping. When synthesized with a mercury-rich surface, HgE QDs display robust n-type doping under ambient conditions, evidenced by band-edge bleaching and intraband absorbance in the mid- to far-IR.[11, 29, 31, 32, 33] Upon treatment with S^{2-}, the electron doping vanishes, yielding intrinsic QDs with no intraband absorbance and recovered interband transitions. The stable doping in mercury-rich HgSe QDs has been utilized to create intraband photodetectors with narrow spectral response in the mid-IR.[11] Recent progress in the synthesis of HgTe QDs has yielded improved colloidal stability and air-stable n-doping, expanding the versatility of these materials for further study.[32]

Here, we observe splitting of the intraband transition in the absorbance of electron-doped HgTe QDs into three peaks. The peak positions of the individual components follow a robust trend with changing nanocrystal size, independent of the QD doping level. We suggest that the intraband absorbance corresponds to transitions between the occupied $1S_e$ state and a series of nondegenerate $1P_e$ states. The strong spin-orbit coupling of HgTe, size uniformity of the synthesized QDs, and deep work function of mercury-rich HgTe QDs allow us to observe this splitting in a colloidal QD solution.

RESULTS AND DISCUSSION

Highly monodisperse HgTe QDs were synthesized using slight modifications to a reported procedure.[32] Briefly, QDs were made by injection of bis(trimethylsilyl)telluride (TMS_2Te) into a hot solution of $HgCl_2$ in oleylamine and growth at mild temperatures (70-120 °C) for 4 to 6 minutes. The QD growth was quenched by injection of anhydrous tetrachloroethylene (TCE), and the QDs were washed with toluene/methanol in a nitrogen glove box. The diameter can be controlled between 5 nm to 13 nm by tuning the injection and growth temperatures and the ratio of Hg to Te precursors. The synthesized QDs have a nearly spherical shape, uniform size, and zinc blende crystal structure, and their absorbance spectra show several clear excitonic transitions (Figures S1-S2). These samples exhibit narrow mid-infrared photoluminescence with a full-width at half-maximum of approximately 80 meV (Figure S3-S4). We found that limiting the time that $HgCl_2$ is kept at elevated temperature in oleylamine and completing all post-synthetic processing in a nitrogen glovebox improved batch to batch reproducibility.

Due to the deep conduction band energy, HgTe QDs are spontaneously electron-doped under ambient conditions.[32] To recover the intrinsic properties of our QDs, we use a mild iodine treatment in TCE to oxidize the doped QDs and yield particles without free electrons (Figure S5, Table S1). This de-doping is not accompanied by an appreciable shift in exciton energies, indicating that the treatment has not changed the QD size.

The absorbance of intrinsic HgTe QDs can be tuned throughout the infrared by controlling the QD size and thus the degree of quantum confinement. Sharp peaks corresponding to molecular vibrations of the solvent and surface-bound organic ligands overlay the characteristic QD

absorbance in the solution spectra (Figure S6), but these peaks can be subtracted to yield spectra with representative QD absorbance. Under our synthetic conditions, the absorbance onset is around 4,000 cm^{-1} (0.5 eV, 2.5 μm) for small nanocrystals of 6 nm in diameter and can reach approximately 1,650 cm^{-1} (0.2 eV, 6.0 μm) at sizes up to 13 nm (Figure 1a). Absorbance further into the infrared can be achieved by particle regrowth upon introduction of additional precursors (Figure S7).[34] Addition of a half equivalent of TMS_2Te to 13 nm QDs at 120 °C yielded 15 nm QDs with an absorbance onset at 1,200 cm^{-1} (0.15 eV, 8.3 μm). Given the large Bohr exciton radius of HgTe (40 nm),[35] size effects on absorbance should be seen up to large nanocrystal sizes, on the order of 100 nm, as recently demonstrated by Lhuillier and colleagues.[36]

Across a range of nanocrystal diameters, three to four clear excitonic features can be resolved in the infrared absorbance spectra of intrinsic HgTe QDs dispersed in TCE (Figure 1). The spectra can be fit using a sum of Gaussians and a parabolic background function (Figure 1b), and the three lowest energy peaks can be assigned to electronic transitions from valence band states to the $1S_e$ and $1P_e$ conduction band states, based on a previously reported tight-binding model.[34, 37] Comparison of the energy of the excitonic transitions for many sizes of intrinsic HgTe QDs reveals a robust trend for each transition with increasing quantum confinement (Figure S8). Notably, the first excitonic feature exhibits a decreased relative oscillator strength as compared to more common QD systems (*e.g.* CdSe[38]), and it gets suppressed as the QD diameter increases. For large QDs, the first absorption feature nearly disappears into a seemingly broad absorption onset; however, this first excitonic feature can be resolved as a clearly defined shoulder in small HgTe (Figure 1a, 6 nm QDs) and becomes clear upon Gaussian fitting for larger nanocrystals (Figure 1b).

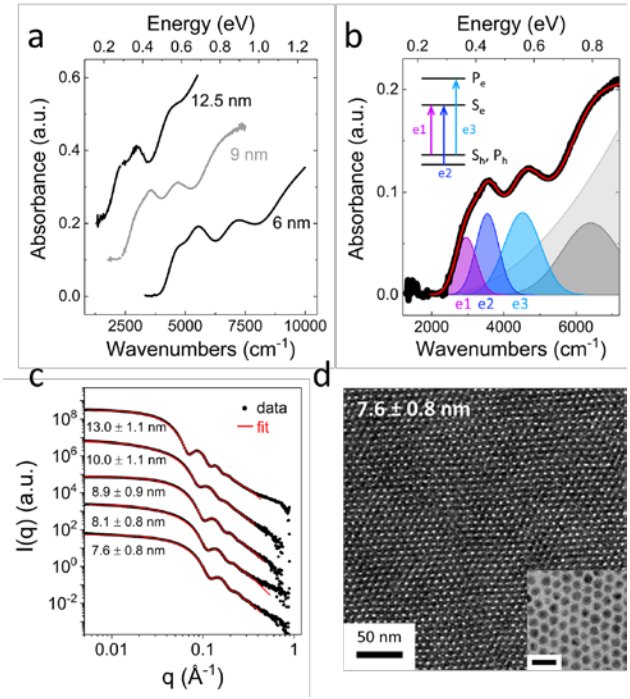

Figure 1. (a) Solution absorbance spectra for three sizes of intrinsic HgTe QDs in TCE show several clear excitonic features and a strong blueshift in the absorption onset with increasing confinement. Infrared absorbance from the solvent (TCE) and ligands (oleylamine) has been subtracted. **(b)** The absorbance spectrum for 9 nm HgTe QDs can be fit with a sum of four Gaussians and a parabolic background. The data is shown as a bold black line, and the fit is shown in red. The inset demonstrates the corresponding electronic transitions for the first three excitonic peaks (e1, e2, and e3). **(c)** SAXS data and corresponding fits for colloidal solutions of HgTe QDs show good size control (~10% distribution) across a range of samples. **(d)** A TEM micrograph shows that HgTe QDs self-assemble into superlattices upon slow evaporation from TCE. The inset shows a monolayer of the same particles drop-cast from a dilute solution (scale bar, 10 nm).

The monodispersity of the HgTe QDs was assessed with small-angle x-ray scattering (SAXS) and self-assembly experiments. SAXS measurements in the 0.005 – 1 $Å^{-1}$ region of momentum

transfer space (q-space) are routinely used to determine the size of colloidal nanoparticles.[39] Size determination from SAXS is preferable to transmission electron microscopy (TEM) size analysis because it is free of selection bias, offering size distribution statistics at the ensemble level. We measured SAXS on solutions of HgTe dispersed in hexane and found that the scattering curves exhibit a characteristic leveling off of the intensity at $q < 1/R_g$ (Guinier region), where R_g is the radius of gyration. This indicates that the particles form dilute-limit colloidal solutions and that the scattering intensity is determined solely by the particles' form factor. The data were further fit using a model-free Maximum Entropy approach to determine the average diameter and size distribution (Figure 1c). The five HgTe samples each have a size polydispersity of approximately 10%, which is on par with well-developed nanocrystal syntheses (*e.g.* CdSe,[40] Pd[41]). For the small QDs (7.6 nm, 8.1 nm, and 8.9 nm), this size distribution was achieved directly from synthesis, but the larger QDs (10.0 nm and 13.0 nm) were size-selected into 4 fractions to improve the monodispersity. Future work could improve the size distribution through more precise temperature modulation and controlled TMS_2Te injection rate or with extensive post-synthetic size selection.

The small size and shape variation of these particles is further demonstrated by their propensity to crystallize into well-ordered superlattices (Figures 1d, S9). Upon slow evaporation of a solution in TCE onto a tilted TEM grid, the QDs self-organize into face-centered cubic (fcc) arrays with ordered domains of several square microns. The diameter of the nanocrystals is directly correlated to the lattice spacing of this array, and we have shown that several sizes of HgTe QDs form fcc superlattices (Figure S9). Monodisperse spheres preferentially crystallize into fcc arrays to maximize their packing density,[42] and the adoption of this structure in our

sample suggests that our QDs plus their bound ligand shell can be approximated as monodisperse spheres.

The high degree of size uniformity of these QDs allows us to observe multiple well-defined features in the intraband absorbance of many samples of n-doped HgTe. As mentioned above, large HgTe QDs synthesized in a mercury-rich solution are spontaneously electron-doped by the environment due to their deep conduction band.[32] With proper surface passivation, this n-doping is air-stable. By introducing electrons into the $1S_e$ state, doping suppresses the first two excitonic transitions and induces a low-energy intraband absorbance corresponding to excitation from the $1S_e$ state to higher conduction band states (Figure 2a-b). This intraband transition can also be observed in the photoluminescence of n-doped QDs (Figure S4), as has been previously demonstrated in n-doped HgS and HgSe QDs.[11, 31, 33] Figure 2a shows a direct comparison of the absorbance spectra for n-doped HgTe QDs under ambient conditions and the same sample after oxidation with molecular iodine. A Gaussian fit of the n-doped QDs demonstrates the strong suppression of the first two excitonic transitions (e1 and e2), corresponding to excitation from valence band states to the $1S_e$ state, and little change in the third excitonic transition (e3), corresponding to excitation from valence band states to the $1P_e$ state (Figure 2b). The intraband absorbance in the n-doped sample spans from 1200 to 2300 cm^{-1} and shows a pronounced dip in the absorbance at ~1550 cm^{-1}. Using a sum of Gaussians, the intraband absorbance can be well-modeled with a minimum of three peaks corresponding to three intraband transitions, i1-i3 (Figure 2b). The dip in the intraband absorbance and shoulder indicating three peaks can be observed at different energies in several sizes of HgTe QDs, confirming that we indeed observe three intraband transitions and not a measurement artifact (Figure 2c). The Gaussian fitting

procedure was applied for many samples of QDs, and the energies of the three intraband transitions show a robust trend with confinement energy (Figure S10).

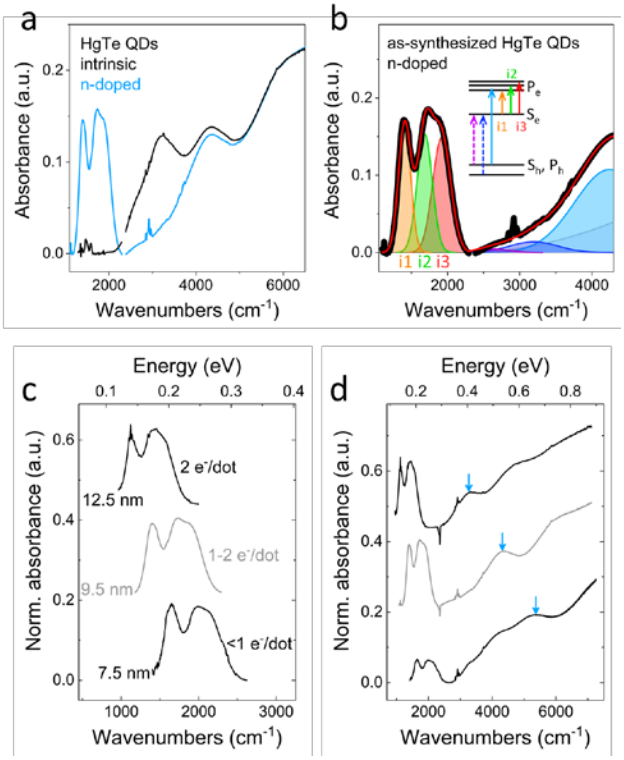

Figure 2. (a) Solution absorbance spectra of HgTe QDs as-synthesized (n-doped) and after treatment with molecular iodine (intrinsic). **(b)** A fit of n-doped HgTe QDs' spectrum to a sum of Gaussians indicates that doping suppresses the first two excitonic transitions (e1, e2) and induces intraband absorbance (i1-i3). The data is a bold black line, and the fit is a red line. **(c)** The intraband absorbance for different sizes of QDs with different doping levels has similar spacing and relative intensity for the three peaks but the peak positions shift with size. **(d)** Comparison of the full absorbance spectra for the samples in **(c)** illustrates the difference in doping for the three samples, based on the difference in relative intensity of the intraband absorbance to the excitonic features. The blue arrows indicate the position of the third excitonic transition (e3).

Here, we observe robust, size-dependent splitting of the intraband features for colloidal QDs under ambient conditions. Studies of chemically n-doped CdSe have shown multiple intraband features in a few select samples and suggested that it may be due to lifting the degeneracy of the P_e state; however, the origin of these features was not studied extensively.[26, 27] Electrochemically doped tetrahedral HgTe QDs prepared under different synthetic conditions show one intraband feature at doping levels up to two electrons per dot and an additional feature at higher doping densities.[43] In our QDs, the split intraband features could be interpreted either as excitations from the $1S_e$ state to a series of nondegenerate $1P_e$ states or as an excitation from $1S_e$ to $1P_e$ and, if the particles are heavily doped, an excitation from $1P_e$ to higher conduction band states. We can determine the influence of doping by comparing the intraband spectra for nanocrystals of different sizes. Larger HgTe QDs have deeper conduction band states because they are less quantum confined, so the as-synthesized QDs are more heavily doped at larger diameters.[32] Figure 2d shows that the relative intensity of the intraband absorbance to the interband absorbance (third exciton, which remains unbleached, marked by a blue arrow) increases at larger sizes, confirming that the larger nanocrystals are more heavily doped.[11] Upon comparison of the normalized intraband spectra (Figure 2c), we see that the peak spacing and relative intensity of the three peaks remain nearly constant at different doping densities, though the absolute position of the peaks shifts with size. We would expect the relative intensity of the three peaks to change with doping density if the transitions did not originate from the same ground state. Therefore, we propose that the observed intraband features correspond to transitions from the $1S_e$ state to a series of nondegenerate $1P_e$ states.

Compilation of the absorbance data for both doped and intrinsic HgTe QDs allows us to construct a more complete understanding of their electronic structure. The energies of the QD transitions (e1-e3, i1-i3) were plotted against the QD diameter determined from SAXS (Figures 4, S11). The diameters obtained from SAXS and the third excitonic position, present in both intrinsic and n-doped QDs, were used to construct a sizing curve for HgTe QDs (Figure S11b). The peak energies indicated by a filled circle were determined from fits of the solution absorbance spectra to a sum of Gaussians and a parabolic background function. Spectra for n-doped QDs were used for the intraband transitions (i1-i3), and spectra for I_2-treated, intrinsic QDs were used for the first and second excitonic transitions (e1, e2). The third excitonic position could be determined from either doped or intrinsic QDs because its position and intensity are largely independent of doping level. The open circles indicate estimated positions of the first and second excitonic transitions for doped QDs based on their linear relationship to the third excitonic energy (see Supporting Information). Both the excitonic and intraband transitions exhibit a monotonic decrease in energy with increasing QD diameter. This confirms that the intraband absorbance correlates to electronic transitions between quantum-confined states.

The change in each transition with size is fit to a function of the form $(a + bd + cd^2)^{-1}$, where d is the diameter (Table S2).[44, 45] Using these equations and the size distribution obtained from SAXS, we can predict the line broadening of each transition due to polydispersity and compare this with our experimental results (Table S3). The width of the first excitonic peak is comparable to other well-developed QD syntheses (~70 meV) and is well estimated by the calculated polydispersity-based peak broadening. Interestingly, the width of the intraband peaks is quite narrow, on the order of 30 meV, and is slightly narrower than our polydispersity-based

broadening calculations, likely due to overestimation of the polydispersity by SAXS because of particle asphericity.[39] Hole-burning experiments on CdSe and InP have previously shown that the homogeneous intraband linewidth can be very narrow, approximately 10 meV at 200K and as low as 3 meV at 10K.[46] This suggests that our ensemble linewidth of the intraband transitions is likely to be broader than the homogeneous intraband linewidth of HgTe QDs due to QD size distribution. The sharp linewidths of the HgTe intraband transitions can be explained as coming from two factors. First, the weak size dependence of the intraband transition energy mitigates polydispersity-related broadening. Second, there is a reduction in fine structure broadening that arises from the nondegeneracy of the P_e states. Each observed peak in the intraband region of the spectrum is related to a transition from $1S_e$ to a single $1P_e$ state.

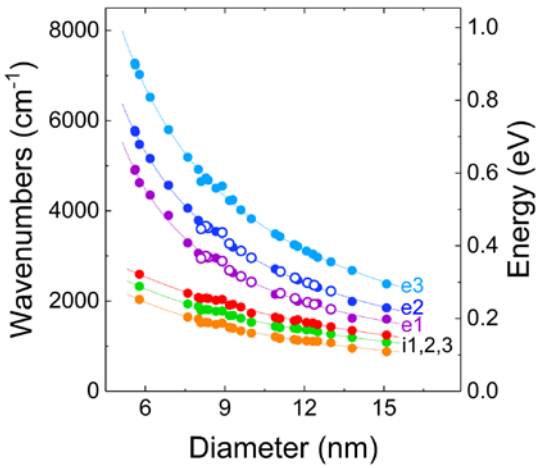

Figure 3. Plot of the peak positions of HgTe QDs as a function of nanocrystal diameter with fits given as a guide for the eye. Diameters are determined from SAXS as described in the Supporting Information. Filled circles indicate peak positions determined from spectral fits to a sum of Gaussians and open circles indicate predicted peak positions as described in the Supporting Information. The intraband points (i1,2,3) for the smallest diameter particles (5.7 nm) were obtained from spectroelectrochemistry, described in the text.

As-synthesized, the maximum doping density that is achieved for a HgTe QD sample is determined by its size and processing conditions and is difficult to precisely control. By using spectroelectrochemistry, we can observe changes in the absorbance of a QD sample at a range of controlled doping densities.[23, 24, 25, 29, 43, 47] In this technique, the absorbance of a QD film is measured under a series of potentials applied in an electrochemical cell. Thus, we can manipulate the Fermi level of a QD film and observe the intraband absorbance and excitonic bleach across a range of doping levels (Figure 4a).

We synthesized a batch of small HgTe QDs (~ 6 nm, Figure S12), such that the intraband absorbance fell in the transparency window of the solvent (propylene carbonate, PC) and electrolyte (tetrabutylammonium perchlorate, TBAP). A film was prepared by drop-casting a concentrated QD solution onto a glass substrate with interdigitated gold electrodes. To make the sample sufficiently conductive, the QDs were cross-linked with ethanedithiol through an on-film ligand exchange.[20] The resulting QD film was placed in a cell with electrolyte solution (PC/TBAP) and pressed against a KBr window to minimize solvent absorbance. A bias was applied to the film using a bipotentiostat with electrochemical potentials monitored with a silver wire pseudoreference. This cell was placed in an FTIR spectrometer, and the absorbance of the film was measured in reflectance mode across a series of applied biases at room temperature. The spectrum of the intrinsic HgTe QD film at 0 V vs Ag/AgCl was taken as a background, and the change in absorbance at a given bias was measured (Figure 4b).

Several features change in the absorbance of the HgTe QDs under negative bias. In the interband region of the spectrum, two bleach features appear which correspond closely to the position of the first two excitonic features in the absorbance spectrum of the as-synthesized QDs (Figure 4c). Additionally, an induced absorbance appears below the first excitonic bleach. At lower energies, we see an induced absorbance with three closely-spaced peaks that matches the intraband absorbance seen in chemically doped QDs. The peak spacing and relative oscillator strength of the three peaks do not change with increasing bias. This suggests that under our experimental conditions we only observe the effects of doping up to two electrons per QD because additional intraband absorbance features should emerge at high bias upon doping of the $1P_e$ level.[43] This further confirms that the three intraband transitions observed in HgTe QDs occur from the first conduction band state ($1S_e$) to a series of closely-spaced excited states. Moreover, the consistent intraband lineshape across the applied bias indicates that electron-electron interactions in QDs doped with two electrons do not have a significant effect on the state energies or transition probability.

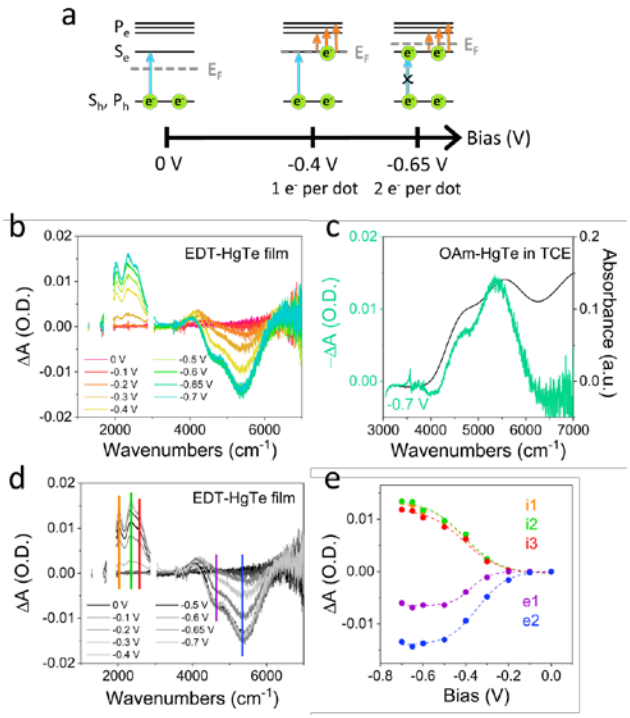

Figure 4. (a) Illustration of the change in the Fermi level (E_F) with applied negative bias and its effect on interband absorbance (blue arrow) and intraband absorbance (orange arrows) of a QD film. **(b)** Difference spectra for a film of EDT-crosslinked HgTe QDs under a series of biases *vs* Ag/AgCl. As a negative bias is applied, an intraband absorbance appears and the first two excitonic features are bleached. **(c)** The bleach in spectroelectrochemistry matches the energy of the first two excitonic features in a solution absorbance measurement of the as-synthesized HgTe QDs. **(e)** The change in absorbance for 3 intraband transitions (i1-i3) and two excitonic bleaches (e1, e2) as a function of applied bias *vs* Ag/AgCl and their corresponding sigmoidal fits, with the position of each transition marked in **(d)** with the corresponding color.

As the bias becomes more negative and the electron doping increases, the magnitude of the excitonic bleach and intraband absorbance increases and then plateaus when the $1S_e$ state is filled with two electrons. As shown previously with CdSe, the change in absorbance as a function of

bias can be modeled to determine the QD band positions.[25, 47] When the Fermi level is aligned with the $1S_e$ state, the state has a 50% probability of being filled with electrons according to Fermi-Dirac statistics. Assuming that the induced absorbance or bleach is directly proportional to the electron occupation, the point at which the Fermi level aligns with the state should be at the midpoint of the intensity increase for the peak in question. Here, the midpoint for each of the observed transitions is approximately -0.4 V *vs* Ag/AgCl, and the point at which the absorbance plateaus, corresponding to full occupation of the $1S_e$ state, is between -0.6 V and -0.65 V (Figure 4d-e). Using cyclic voltammetry, we confirmed that the $1S_e$ state contains one electron at approximately -0.4 V *vs* Ag/AgCl and two electrons at approximately -0.65 V (Figure S13).

To understand the observed splitting of the $1P_e$ state in HgTe QDs, we modeled the intraband absorbance using a well-established tight-binding model.[12, 37] We found that for highly symmetric particle shapes, spheres and octahedra (Figures 5a, S14), the intraband absorbance is split into two peaks due to spin-orbit coupling. To account for the additional splitting of the higher energy peak observed experimentally, we considered the effect of lower symmetry confinement potentials. For asymmetric particle shapes, oblate ellipsoids and truncated cubes with unequal truncations, we predict splitting of the intraband absorbance into three peaks that closely mimics experimental results (Figures 5b-c, S14). Moreover, the predicted intraband peak positions for many sizes of truncated cubes follow the size trends observed experimentally (Figure 5e). Thus, the $1P_e$ level is split primarily by strong spin-orbit coupling and additionally split by asymmetry that breaks the degeneracy of the x, y, and z axes (Figure 5d). Based on close examination of high resolution TEM images, our HgTe QDs are reasonably modeled as a low-

symmetry near-sphere like a truncated cube (Figure S15). Our TEM images also reveal planar defects which could account for the reduction of symmetry in the confinement potential.

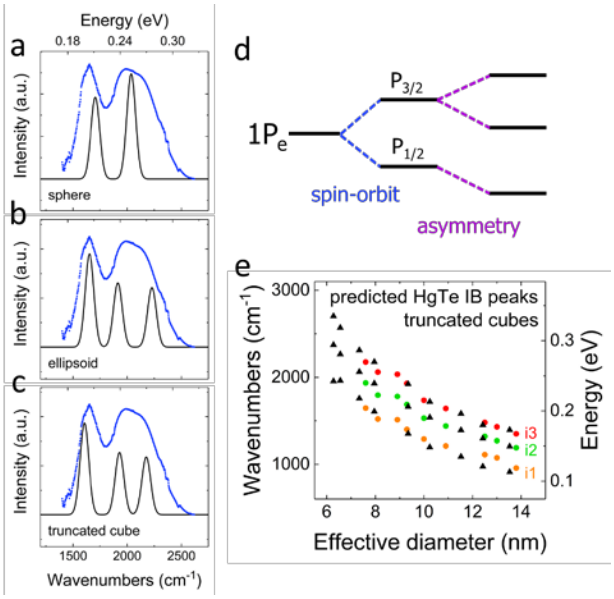

Figure 5. (a-c) Predicted intraband absorbance spectra (black lines) for several shapes of HgTe QDs with a volume equal to a sphere with a radius of 4 nm and comparison with experimental data for a solution of 7.6 nm diameter QDs (blue points). **(d)** Schematic demonstrating the splitting of the P_e state by both spin-orbit coupling and structural asymmetry. **(e)** Comparison of predicted intraband peaks (black triangles) for many sizes of truncated cubes and experimental data (colorful circles). The size is given as the effective diameter of a sphere with volume equal to that of the modeled truncated cube.

CONCLUSIONS

We have demonstrated direct spectroscopic evidence of conduction band fine structure in electron-doped HgTe QDs. Robust splitting of the intraband absorbance into three peaks is observed across many QD samples with different confinement and doping levels. This splitting can only be observed for monodisperse QDs (Figure S16), where the absorbance linewidths are

narrow and the overlap between peaks is minimized. Furthermore, spectroelectrochemical measurements reveal that the peak spacing and relative oscillator strengths of the three peaks do not change appreciably with doping level. The three peaks seen in the intraband spectra correspond to transitions from the lowest conduction band state, $1S_e$, to a series of three nondegenerate $1P_e$ states. The significant splitting into two well-defined peaks can be rationalized by spin-orbit coupling, which is much more pronounced for heavy metal tellurides than for the analogous selenides or sulfides. Thus, split intraband peaks were not observed in previous studies of n-doped HgS or HgSe.[29, 31, 33] The intraband spectra can be well-modeled by a sum of three Gaussian peaks, suggesting that there is additional splitting of the $1P_e$ state. This may be rationalized by structural asymmetry of the particles which breaks the degeneracy of x, y, and z.

MATERIALS AND METHODS

Materials. $HgCl_2$ (≥ 98%), iodine (99.99 %), 1,2-ethanedithiol (≥98.0% (GC)), HCl (ACS reagent, 37%), isopropanol (≥99.7%, FG), tetrabutylammonium perchlorate (for electrochemical analysis, ≥99.0%) and anhydrous solvents (tetrachloroethylene, hexane, toluene, propylene carbonate, and methanol) were purchased from Sigma Aldrich and used as received. Oleylamine (technical grade, 70 %) was purchased from Sigma Aldrich and purified before use by freezing, thawing, and then centrifuging to remove any insoluble solids. The purified oleylamine was dried under dynamic vacuum at 120 °C for two to three hours and stored in a nitrogen glove box. Bis(trimethylsilyl)telluride (98 %) was purchased from Acros and stored frozen in a nitrogen glove box.

HgTe synthesis. HgTe quantum dots (QDs) were synthesized based on a previously reported method.[32] A portion of 135 mg $HgCl_2$ (0.5 mmol, stored under N_2) and 16 mL oleylamine (OAm) were heated to 120 °C under nitrogen and briefly degassed. The solution was then put under nitrogen and cooled to the desired temperature for nanocrystal growth (70 – 120 °C, larger nanocrystals obtained at higher temperature). Meanwhile, a solution of 68 mg bis(trimethylsilyl)telluride (TMS_2Te, 0.25 mmol) in 5 mL OAm was prepared in a N_2 glove box. The TMS_2Te solution was injected into the $HgCl_2$ solution and heated at the injection temperature for 4-6 minutes. The reaction was quickly cooled by injection of 20 mL of anhydrous tetrachloroethylene (TCE) and cooled to room temperature either under ambient conditions or in a water bath. This reaction can be easily scaled up to 1 mmol HgTe by using 543 mg $HgCl_2$ (2 mmol), 50 mL OAm, 274 mg TMS_2Te (1 mmol) in 10 mL OAm, and 40 mL TCE. To synthesize HgTe QDs larger than 11 nm, the $HgCl_2$ to TMS_2Te molar ratio was increased to 4:1. Up to 13 nm, the other reaction conditions were maintained, but for larger QDs, additional TMS_2Te (half an equivalent) was diluted in OAm and added dropwise after the initial growth. The temperature was maintained for two minutes after the TMS_2Te addition, and then the reaction was quenched with TCE. *[Note: Some elemental mercury is produced during this reaction. Prolonged evacuation at elevated temperature or heating above 120 °C produces more elemental mercury.]*

Purification and storage of the HgTe QDs were performed in a nitrogen glove box. The QDs were isolated by addition of methanol nonsolvent and centrifugation. The QDs were further washed twice by dissolution into toluene plus 5 vol% OAm and precipitation with methanol and centrifugation. Improved monodispersity could be achieved by size-selective precipitation,

where methanol or ethanol nonsolvent was gradually added and particles with smaller diameter were successively removed by centrifugation. The resulting QDs were dispersed in TCE for optical measurements.

*Optical absorption***.** UV-vis-NIR spectra were collected with a Cary 5000 spectrophotometer. Infrared spectra were collected with a Thermo Nexus 670 FTIR in transmission mode using a sandwich cell with CaF_2 windows and a 0.5 mm pathlength. Spectra for oxidized NCs were obtained by adding ~20 μL of 0.05 M I_2 solution in TCE to a concentrated NC solution (~10 mg/mL) and measuring either immediately or within a few hours. Longer wait times after iodine addition led to less oxidized samples and/or etching of the NCs.

Transmission electron microscopy (TEM). TEM images were obtained on an FEI Technai F30 microscope at 300 kV. Superlattices were prepared by the tilted evaporation method, where a NC solution in TCE is slowly evaporated over a tilted carbon-coated copper TEM grid.[48]

Photoluminescence (PL). PL samples were prepared as drop-cast films on a ZnSe window and, if necessary, treated with ammonium sulfide to de-dope the QDs. The films were photoexcited by an 808 nm continuous laser chopped at 100 kHz. The photoluminescence was measured with a step-scan FTIR with an MCT detector and a lock-in amplifier. The PL intensity at different wavelengths is normalized by taking the ratio of the signal from a blackbody source to the calculated blackbody spectrum at its temperature.

Small-angle x-ray scattering (SAXS). SAXS measurements were conducted at the XSD-CMS 12-ID-B beamline at the Advanced Photon Source, Argonne National Laboratory. The beamline energy was fixed at 13.3 keV. SAXS measurements were also collected on a SAXSLab Ganesha in-house instrument using Cu Kα radiation. The SAXS curves were analyzed by fitting a quantitative model in Igor Pro using the Irena package (available at http://usaxs.xray.aps.anl.gov/staff/ilavsky/irena.html).[49] The scattering curves were fit in the particle size distribution module using the model-free Maximum Entropy approach. Based on TEM data, the particles' form factor was assumed to be that of a sphere with an aspect ratio of 1. The extracted size distributions were further fit with symmetric Gaussians.

Spectroelectrochemistry. HgTe QD solutions in TCE were dropcast on Au interdigitated electrodes (IDE), crosslinked with a 1:1:50 solution of ethanedithiol (EDT) / HCl / isopropanol (IPA), and rinsed with IPA. The IDE is on glass with spacing d = 20μm and finger width d_0 = 10 μm. The spectroelectrochemical cell is assembled and filled with 0.1M tetrabutylammonium perchlorate (TBAP) / propylene carbonate (PC) in air. The sample electrode is pressed lightly against the KBr window of the cell to minimize the infrared absorption from the electrolyte. Then the cell is put in the Fourier transform infrared spectrometer (Nicolet Magna IR 550). After flushing with N_2 for several hours, infrared spectra are measured in reflectance. We first characterize the cyclic voltammetry and the film conductance with a bi-potentiostat. Then, we set the potential at the minimum conductance position where the QDs are undoped. The undoped spectrum is taken as the background. Spectra at other potentials are taken with respect to the undoped spectrum. All preparation and measurements are done at room temperature.

Theory methods. We have performed atomistic tight-binding electronic structure calculations following the methodology described in Ref. 35.[37] The single-particle tight-binding Hamiltonian matrix is written in a basis of $sp^3d^5s^*$ orbitals (for the two spin orientations) on each Hg or Te atom. We employ the tight-binding parameters that describe HgTe at 300K. The surfaces of the QDs are saturated by pseudo-hydrogen atoms in order to avoid surface states. Due to the large size of the QDs, only the eigenstates in the vicinity of the bandgap region are calculated.[50]

We considered two situations where the QDs contain either one or two additional electrons. In the case of QDs charged with one electron, single-particle states can be used directly to calculate the oscillator strengths for the intraband optical transitions. For the sake of comparison with experiments, each optical transition line is broadened using a Lorentzian function $L(\omega)=\eta/((\omega^2+\eta^2))$ where η is a parameter (5 meV).

In the case of QDs containing two electrons, we calculate the two-particle states using a configuration-interaction (CI) method.[51, 52] In the first step, we calculate the self-energy corrections to the single-particle energies induced by the dielectric polarization of the QD following the injection of the separate electrons. In the second step, the screened Coulomb electron-electron interaction is introduced into the two-particle Hamiltonian which is written in the basis of Slater determinants built from the tight-binding single-particle states. In the present case, it is found that the transition energies calculated using single-particle or two-particle states are very close. Correlation effects are weak because of the combination of strong quantum confinement and high dielectric screening in HgTe QDs.

ASSOCIATED CONTENT

Supporting Information

Additional figures (Figure S1-S16) and tables (Table S1-S3) are given in the Supporting Information. This material is available free of charge *via* the Internet at http://pubs.acs.org.

The authors declare no competing financial interests.

AUTHOR INFORMATION

Corresponding Author

dvtalapin@uchicago.edu

ACKNOWLEDGMENTS

This work was supported by the University of Chicago Materials Research Science and Engineering Center, which is funded by the NSF under award number DMR-1420709, by the NSF under award number CHE-1611331, and by the Defense Advanced Research Projects Agency (DARPA) as a subcontract to Voxtel, Inc. for the Wired program. This work used resources of the Advanced Photon Source, a U.S. Department of Energy (DOE) Office of Science User Facility operated for the DOE Office of Science by Argonne National Laboratory under Contract No. DE-AC02-06CH11357.

REFERENCES

1. Oh, N.; Kim, B. H.; Cho, S.-Y.; Nam, S.; Rogers, S. P.; Jiang, Y.; Flanagan, J. C.; Zhai, Y.; Kim, J.-H.; Lee, J.; Yu, Y.; Cho, Y. K.; Hur, G.; Zhang, J.; Trefonas, P.; Rogers, J. A.; Shim, M., Double-Heterojunction Nanorod Light-Responsive LEDs for Display Applications. *Science* **2017,** *355*, 616-619.
2. Zhang, H.; Chen, S.; Sun, X. W., Efficient Red/Green/Blue Tandem Quantum-Dot Light-Emitting Diodes with External Quantum Efficiency Exceeding 21%. *ACS Nano* **2018,** *12*, 697-704.
3. Mashford, B. S.; Stevenson, M.; Popovic, Z.; Hamilton, C.; Zhou, Z.; Breen, C.; Steckel, J.; Bulovic, V.; Bawendi, M.; Coe-Sullivan, S.; Kazlas, P. T., High-Efficiency Quantum-Dot Light-Emitting Devices with Enhanced Charge Injection. *Nat. Photonics* **2013,** *7*, 407.
4. Semonin, O. E.; Luther, J. M.; Choi, S.; Chen, H.-Y.; Gao, J.; Nozik, A. J.; Beard, M. C., Peak External Photocurrent Quantum Efficiency Exceeding 100% *via* MEG in a Quantum Dot Solar Cell. *Science* **2011,** *334*, 1530-1533.
5. Lan, X.; Voznyy, O.; García de Arquer, F. P.; Liu, M.; Xu, J.; Proppe, A. H.; Walters, G.; Fan, F.; Tan, H.; Liu, M.; Yang, Z.; Hoogland, S.; Sargent, E. H., 10.6% Certified Colloidal Quantum Dot Solar Cells *via* Solvent-Polarity-Engineered Halide Passivation. *Nano Lett.* **2016,** *16*, 4630-4634.
6. Du, J.; Du, Z.; Hu, J.-S.; Pan, Z.; Shen, Q.; Sun, J.; Long, D.; Dong, H.; Sun, L.; Zhong, X.; Wan, L.-J., Zn–Cu–In–Se Quantum Dot Solar Cells with a Certified Power Conversion Efficiency of 11.6%. *J. Am. Chem. Soc.* **2016,** *138*, 4201-4209.
7. Wu, K.; Li, H.; Klimov, V. I., Tandem Luminescent Solar Concentrators Based on Engineered Quantum Dots. *Nat. Photonics* **2018,** *12*, 105-110.
8. Coropceanu, I.; Bawendi, M. G., Core/Shell Quantum Dot Based Luminescent Solar Concentrators with Reduced Reabsorption and Enhanced Efficiency. *Nano Lett.* **2014,** *14*, 4097-4101.
9. Liu, W.; Chang, A. Y.; Schaller, R. D.; Talapin, D. V., Colloidal InSb Nanocrystals. *J. Am. Chem. Soc.* **2012,** *134*, 20258-20261.
10. Murray, C. B.; Sun, S.; Gaschler, W.; Doyle, H.; Betley, T. A.; Kagan, C. R., Colloidal Synthesis of Nanocrystals and Nanocrystal Superlattices. *Ibm J Res Dev* **2001,** *45*, 47-56.
11. Deng, Z.; Jeong, K. S.; Guyot-Sionnest, P., Colloidal Quantum Dots Intraband Photodetectors. *ACS Nano* **2014,** *8*, 11707-11714.
12. Keuleyan, S. E.; Guyot-Sionnest, P.; Delerue, C.; Allan, G., Mercury Telluride Colloidal Quantum Dots: Electronic Structure, Size-Dependent Spectra, and Photocurrent Detection up to 12 μm. *ACS Nano* **2014,** *8*, 8676-8682.
13. Keuleyan, S.; Lhuillier, E.; Guyot-Sionnest, P., Synthesis of Colloidal HgTe Quantum Dots for Narrow Mid-IR Emission and Detection. *J. Am. Chem. Soc.* **2011,** *133*, 16422-16424.
14. Srivastava, V.; Janke, E. M.; Diroll, B. T.; Schaller, R. D.; Talapin, D. V., Facile, Economic and Size-Tunable Synthesis of Metal Arsenide Nanocrystals. *Chemistry of Materials* **2016,** *28*, 6797-6802.
15. Harris, D. K.; Allen, P. M.; Han, H.-S.; Walker, B. J.; Lee, J.; Bawendi, M. G., Synthesis of Cadmium Arsenide Quantum Dots Luminescent in the Infrared. *J. Am. Chem. Soc.* **2011,** *133*, 4676-4679.
16. Piepenbrock, M.-O. M.; Stirner, T.; Kelly, S. M.; O'Neill, M., A Low-Temperature Synthesis for Organically Soluble HgTe Nanocrystals Exhibiting Near-Infrared Photoluminescence and Quantum Confinement. *J. Am. Chem. Soc.* **2006,** *128*, 7087-7090.

17. Kovalenko, M. V.; Kaufmann, E.; Pachinger, D.; Roither, J.; Huber, M.; Stangl, J.; Hesser, G.; Schäffler, F.; Heiss, W., Colloidal HgTe Nanocrystals with Widely Tunable Narrow Band Gap Energies: From Telecommunications to Molecular Vibrations. *J. Am. Chem. Soc.* **2006,** *128*, 3516-3517.
18. Rogach, A.; Kershaw, S. V.; Burt, M.; Harrison, M. T.; Kornowski, A.; Eychmüller, A.; Weller, H., Colloidally Prepared HgTe Nanocrystals with Strong Room-Temperature Infrared Luminescence. *Advanced Materials* **1999,** *11*, 552-555.
19. Keuleyan, S.; Lhuillier, E.; Brajuskovic, V.; Guyot-Sionnest, P., Mid-Infrared HgTe Colloidal Quantum Dot Photodetectors. *Nat. Photonics* **2011,** *5*, 489.
20. Guyot-Sionnest, P.; Roberts, J. A., Background Limited Mid-Infrared Photodetection with Photovoltaic HgTe Colloidal Quantum Dots. *Appl. Phys. Lett.* **2015,** *107*, 253104.
21. Ackerman, M. M.; Tang, X.; Guyot-Sionnest, P., Fast and Sensitive Colloidal Quantum Dot Mid-Wave Infrared Photodetectors. *ACS Nano* **2018**.
22. Tang, X.; Ackerman, M. M.; Guyot-Sionnest, P., Thermal Imaging with Plasmon Resonance Enhanced HgTe Colloidal Quantum Dot Photovoltaic Devices. *ACS Nano* **2018**.
23. Wehrenberg, B. L.; Guyot-Sionnest, P., Electron and Hole Injection in PbSe Quantum Dot Films. *J. Am. Chem. Soc.* **2003,** *125*, 7806-7807.
24. Yu, D.; Wang, C.; Guyot-Sionnest, P., n-Type Conducting CdSe Nanocrystal Solids. *Science* **2003,** *300*, 1277.
25. Wang, C.; Shim, M.; Guyot-Sionnest, P., Electrochromic Nanocrystal Quantum Dots. *Science* **2001,** *291*, 2390-2392.
26. Shim, M.; Guyot-Sionnest, P., n-type Colloidal Semiconductor Nanocrystals. *Nature* **2000,** *407*, 981.
27. Rinehart, J. D.; Schimpf, A. M.; Weaver, A. L.; Cohn, A. W.; Gamelin, D. R., Photochemical Electronic Doping of Colloidal CdSe Nanocrystals. *J. Am. Chem. Soc.* **2013,** *135*, 18782-18785.
28. Schimpf, A. M.; Ochsenbein, S. T.; Buonsanti, R.; Milliron, D. J.; Gamelin, D. R., Comparison of Extra Electrons in Colloidal n-Type Al3+-Doped and Photochemically Reduced ZnO Nanocrystals. *Chem. Commun.* **2012,** *48*, 9352-9354.
29. Jeong, K. S.; Deng, Z.; Keuleyan, S.; Liu, H.; Guyot-Sionnest, P., Air-Stable n-Doped Colloidal HgS Quantum Dots. *J. Phys. Chem. Lett.* **2014,** *5*, 1139-1143.
30. Robin, A.; Livache, C.; Ithurria, S.; Lacaze, E.; Dubertret, B.; Lhuillier, E., Surface Control of Doping in Self-Doped Nanocrystals. *ACS Appl. Mater. Interfaces* **2016,** *8*, 27122-27128.
31. Deng, Z.; Guyot-Sionnest, P., Intraband Luminescence from HgSe/CdS Core/Shell Quantum Dots. *ACS Nano* **2016,** *10*, 2121-2127.
32. Shen, G.; Chen, M.; Guyot-Sionnest, P., Synthesis of Nonaggregating HgTe Colloidal Quantum Dots and the Emergence of Air-Stable n-Doping. *J. Phys. Chem. Lett.* **2017**, 2224-2228.
33. Shen, G.; Guyot-Sionnest, P., HgS and HgS/CdS Colloidal Quantum Dots with Infrared Intraband Transitions and Emergence of a Surface Plasmon. *J. Phys. Chem. C* **2016,** *120*, 11744-11753.
34. Keuleyan, S.; Kohler, J.; Guyot-Sionnest, P., Photoluminescence of Mid-Infrared HgTe Colloidal Quantum Dots. *J. Phys. Chem. C* **2014,** *118*, 2749-2753.
35. Grahn, H. T., *Introduction to Semiconductor Physics*. World Scientific: 1999.

36. Goubet, N.; Jagtap, A.; Livache, C.; Martinez, B.; Portalès, H.; Xu, X. Z.; Lobo, R. P. S. M.; Dubertret, B.; Lhuillier, E., Terahertz HgTe Nanocrystals: Beyond Confinement. *J. Am. Chem. Soc.* **2018**.
37. Allan, G.; Delerue, C., Tight-Binding Calculations of the Optical Properties of HgTe Nanocrystals. *Phys. Rev. B* **2012,** *86*, 165437.
38. Murray, C. B.; Norris, D. J.; Bawendi, M. G., Synthesis and Characterization of Nearly Monodisperse CdE (E = Sulfur, Selenium, Tellurium) Semiconductor Nanocrystallites. *Journal of the American Chemical Society* **1993,** *115*, 8706-8715.
39. Li, T.; Senesi, A. J.; Lee, B., Small Angle X-ray Scattering for Nanoparticle Research. *Chem. Rev.* **2016,** *116*, 11128-11180.
40. Mattoussi, H.; Cumming, A. W.; Murray, C. B.; Bawendi, M. G.; Ober, R., Characterization of CdSe Nanocrystallite Dispersions by Small Angle X-ray Scattering. *J. Chem. Phys.* **1996,** *105*, 9890-9896.
41. Wu, L.; Lian, H.; Willis, J. J.; Goodman, E. D.; McKay, I. S.; Qin, J.; Tassone, C. J.; Cargnello, M., Tuning Precursor Reactivity toward Nanometer-Size Control in Palladium Nanoparticles Studied by *in Situ* Small Angle X-ray Scattering. *Chem. Mater.* **2018,** *30*, 1127-1135.
42. Boles, M. A.; Engel, M.; Talapin, D. V., Self-Assembly of Colloidal Nanocrystals: From Intricate Structures to Functional Materials. *Chem. Rev.* **2016,** *116*, 11220-11289.
43. Liu, H.; Keuleyan, S.; Guyot-Sionnest, P., n- and p-Type HgTe Quantum Dot Films. *J. Phys. Chem. C* **2012,** *116*, 1344-1349.
44. de Mello Donegá, C.; Koole, R., Size Dependence of the Spontaneous Emission Rate and Absorption Cross Section of CdSe and CdTe Quantum Dots. *J. Phys. Chem. C* **2009,** *113*, 6511-6520.
45. Allan, G.; Delerue, C., Confinement Effects in PbSe Quantum Wells and Nanocrystals. *Phys. Rev. B* **2004,** *70*, 245321.
46. Shim, M.; Guyot-Sionnest, P., Intraband Hole Burning of Colloidal Quantum Dots. *Phys. Rev. B* **2001,** *64*, 245342.
47. Spittel, D.; Poppe, J.; Meerbach, C.; Ziegler, C.; Hickey, S. G.; Eychmüller, A., Absolute Energy Level Positions in CdSe Nanostructures from Potential-Modulated Absorption Spectroscopy (EMAS). *ACS Nano* **2017,** *11*, 12174-12184.
48. Bodnarchuk, M. I.; Kovalenko, M. V.; Heiss, W.; Talapin, D. V., Energetic and Entropic Contributions to Self-Assembly of Binary Nanocrystal Superlattices: Temperature as the Structure-Directing Factor. *J. Am. Chem. Soc.* **2010,** *132*, 11967-11977.
49. Jan, I.; R., J. P., Irena: Tool Suite for Modeling and Analysis of Small-Angle Scattering. *Journal of Applied Crystallography* **2009,** *42*, 347-353.
50. Niquet, Y. M.; Delerue, C.; Allan, G.; Lannoo, M., Method for Tight-Binding Parametrization: Application to Silicon Nanostructures. *Phys. Rev. B* **2000,** *62*, 5109-5116.
51. Delerue, C.; Lannoo, M., *Nanostructures: Theory and Modelling*. Springer: 2004.
52. Martin, E.; Delerue, C.; Allan, G.; Lannoo, M., Theory of Excitonic Exchange Splitting and Optical Stokes Shift in Silicon Nanocrystallites: Application to Porous Silicon. *Phys. Rev. B* **1994,** *50*, 18258-18267.